THE JOURNAL OF PHYSICAL CHEMISTRY C

Article

pubs.acs.org/JPCC

Operando Effects on the Structure and Dynamics of $Pt_nSn_m/\gamma\text{-}Al_2O_3$ from Ab Initio Molecular Dynamics and X-ray Absorption Spectra

Fernando D. Vila,[†] John J. Rehr,*[,†] Shelly D. Kelly,[‡] and Simon R. Bare[‡]

[†]Department of Physics, University of Washington, Seattle, Washington 98195, United States

[‡]UOP LLC, a Honeywell Company, Des Plaines, Illinois 60016, United States

Supporting Information

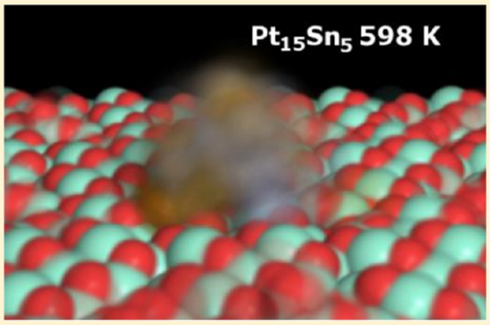

ABSTRACT: Alumina-supported Pt−Sn nanocluster catalysts are widely used in reforming processes, yet a theoretical understanding of their structure and function is far from complete. In an attempt to elucidate their behavior under operando conditions, we have carried out a detailed investigation of nanoscale bimetallic clusters of Pt and Sn supported on γ-Al_2O_3 using a combination of finite temperature ab initio molecular dynamics and theoretical X-ray absorption spectroscopy (XAS). Our simulations reveal a rich nonequilibrium structure over several time scales, with vibrational and anomalous structural disorder and fluctuating charge transfer to the support. In contrast with bulk Pt−Sn materials, the clusters are found to be markedly inhomogeneous, with substantial differences between surface and internal structure. The Sn atoms are preferentially segregated to the surface and fluctuate between different Pt bonds over a picosecond time scale. Importantly, these properties show how an improved XAS analysis of these systems should take into account both their inhomogeneity and dynamic structural disorder. Although our study is limited to small nanoclusters due to the limitations of ab initio molecular dynamics, we argue that their unusual dynamical structure also has important implications for catalytic behavior of these systems, which is briefly illustrated by the adsorption and dissociation reactivity of H_2.

INTRODUCTION

Alumina-supported bimetallic reforming catalysts have been a stalwart of the petroleum reforming industry for the production of aromatic hydrocarbons in fuels over the last several decades.[1,2] The Pt−Sn bimetallic system is one of the more important and is widely used in commercial refining units, especially in continuous regeneration units.[3,4] It has been reported that the addition of Sn to Pt decreases the hydrogenolysis activity of Pt, improves the stability of the catalyst against deactivation by coke deposition, and aids in preventing sintering of the nanoparticles (see references in ref 5). The two main effects of adding Sn to Pt have been described as: (i) an ensemble effect, where the number of contiguous Pt atoms is diluted by Sn, thus preventing reactions requiring multiple Pt atoms, and (ii) an electronic effect, where the electronic structure of the Pt is modified by alloying with Sn.

Given the commercial importance of Pt−Sn catalysts, they have been the subject of several investigations. These studies have shown, for example, that the structure of the Pt−Sn nanoparticles is dependent on the support, the preparation procedure, the weight loading of each metal, and the reduction temperature. These catalysts have been studied using a range of techniques. In particular, X-ray absorption spectroscopy (XAS) has proved to be a powerful technique to investigate their element specific electronic and structural properties because their metal loadings are in the fractions of a weight percent and highly dispersed on the support.[2,6] Focusing on alumina-supported Pt−Sn catalysts, early XAFS (X-ray absorption fine structure) investigations[6,8] concluded that there is a significant interaction between the Pt and Sn as the platinum is more highly dispersed than without Sn and that the form of the clusters consisted of platinum clusters dispersed on the alumina with Sn^{2+} present at the support surface. Caballero et al.,[7] using organometallic precursors to increase the degree of interaction between the metals, also concluded that the XAFS spectra were best understood assuming dispersed Pt−Sn nanoparticles that are stabilized on the alumina surface through Pt−O−Sn^{2+} bonds. In contrast, Iglesias-Juez et al.[8] suggested from their XAFS data that the Sn atoms are preferentially located at the surface of the Pt nanoparticles. Nevertheless, because XAS yield results that are both time-averaged and number-averaged over a particular absorber, a clear picture of local cluster structure and dynamics from such studies is lacking and can be inferred only from ad hoc models.[9]

From the theoretical perspective, Pt−Sn nanoclusters supported on alumina have been relatively unexplored. Recently Jahel et al.[10] presented ground-state density functional theory (DFT) calculations of Pt_xSn_{13-x} clusters, with $x = 13$, 7, and 0, both isolated and supported on a γ-Al_2O_3 (100) surface.

Received: April 20, 2013
Revised: May 21, 2013
Published: May 28, 2013

dx.doi.org/10.1021/jp403931z | *J. Phys. Chem. C* 2013, 117, 12446−12457

They find that the system is stabilized by flattening the cluster into a biplanar structure. This agrees with results for unalloyed Pt_{10} clusters,[11] where the nanoparticles are observed to form two layers, one with oxide characteristics in contact with the support and a metallic layer above.

However, the above studies, both experimental and theoretical, are largely in terms of static structures. The characterization was performed at either liquid nitrogen temperature or room temperature (RT) after in situ reduction of the catalyst. This of course begs the question to what extent the conclusions continue to be relevant when the catalytic chemistry is performed at elevated, operando temperatures (OTs). We have previously shown for small supported Pt nanoclusters that dynamical, nonequilibrium properties are of crucial importance in this regime. Moreover, they can be elucidated by a combination of finite temperature DFT molecular dynamics (DFT/MD) and XAS simulations.[11,12] For example, we showed that unusual operando phenomena such as large structural disorder and negative thermal expansion (NTE) arise from dynamic behavior and the interplay between charge-transfer and entropic effects. Indeed these unusual properties were explained semiquantitatively by DFT/MD and XAS simulations. These phenomena are driven by large, dynamical fluctuations and fluxional bonding in the structure.[11]

In an effort to understand these dynamic effects in representative Pt−Sn nanocatalysts, we now apply finite-temperature DFT/MD and XANES calculations to 20-atom nanoscale bimetallic clusters, $Pt_{10}Sn_{10}$ and $Pt_{15}Sn_5$, supported on the (110) surface of γ-Al_2O_3. DFT/MD is important for this study, as conventional MD with ad hoc pair potentials cannot capture all of the observed nonequilibrium effects. Although small and lacking much of the complexity of real catalysts for computational simplicity, our findings are also applicable to much larger systems. Our primary objective is to garner an atomistic understanding of their unusual structural and physicochemical properties under operando conditions, that is, at high temperatures. A secondary objective is to understand how these characteristics might affect the reactivity of adsorbed molecules under these conditions. We find that the fraction of Sn dramatically affects the structure, dynamics, and electronic properties of these systems and therefore has important implications for their catalytic properties. In particular, we find that the Sn atoms are preferentially segregated to the cluster surface and support. Given the sensitivity of catalytic properties to the particle surface, our results show that it is especially important to view the cluster structure in terms of their surface, cluster−support interaction, and internal compositions rather than their global average structure. Thus conventional XAS analysis techniques that ignore inhomogeneity and fluctuating disorder can be misleading. In contrast, results of our DFT/MD simulations suggest how the inhomogeneity and dynamical structure can be characterized and modeled, thus leading to a more quantitative analysis of XAS experiments and better understanding of these nanocatalysts.

■ COMPUTATIONAL DETAILS

Ab initio DFT/MD simulations of nanoscale Pt−Sn alloy clusters on γ-Al_2O_3 were carried out at two temperatures: 298 (RT) and 598 K, which is typical of OTs using the DFT-based VASP code.[13] All VASP simulations were performed at the Γ point, using the PBE functional and a plane-wave cutoff of 396 eV. As demonstrated in ref 11, this level of theory is adequate to explain at least semiquantitatively the nonequilibrium behavior of nanoclusters. Although PBE leads to slightly softer and longer bonds than typically measured, this difference should not have a significant effect on the dynamical behavior in these nanoclusters. To investigate the effect of composition, we used clusters with the same total number of atoms (20) and different Pt:Sn ratios: $Pt_{10}Sn_{10}$ (1:1) and $Pt_{15}Sn_5$ (3:1). The chosen cluster size is consistent with a broad range of "real" reforming catalysts, while the Pt:Sn ratios correspond to the stable phases in the Pt−Sn bulk alloy phase diagram.[14−16] Initial structures for the clusters were obtained by randomly substituting Sn atoms into the global minima of the gas-phase Pt_{20} cluster and then placing the resulting structures onto the "d" layer of the dehydroxylated [110] surface of γ-Al_2O_3.[17] This surface is represented by four layers (two frozen and two fully relaxed) with 64 Al and 96 O atoms. Of course, in real catalysts, the substrate of the alumina will be partially hydroxylated, contain defects, and likely also have chloride adsorbed, effects which have only recently been treated in DFT calculations.[18] However, because much of the Sn is segregated to the cluster surface, these effects may not strongly affect our conclusions. The addition of these additional substrate complexities will be the subject of future work.[18] The size of the surface supercells is 19.4 Å × 13.7 Å, thus ensuring proper separation between images. The surface slabs are repeated every 20.0 Å with an effective ∼16 Å of vacuum separation. To sample long time scales, we have followed the common procedure of including several parallel calculations with independent trajectories. To this end, four of these random clusters were subsequently relaxed to their optimal ground-state conformations, and these conformations were used to start several RT simulations. The initial structures for the OT runs were obtained by randomly sampling and quenching four conformations from the RT trajectories. All DFT/MD simulations in this work used a time step of 3 fs, which is adequate to capture the "fast" bond vibrations of the system. After an initial 3 ps period, which is adequate to allow for thermalization, a subsequent 8 ps period was used to acquire statistical averages.

This net time scale of $4 \times 8 = 32$ ps is long compared with the mean fluctuations of the center of mass (CM) of about 2 to 3 ps and still moderate compared to longer time-scale processes such as bond-breaking between the cluster and the substrate, which are on the order of 10−20 ps. Thus the use of four different trajectories roughly samples this longer time motion and is found to be adequate to generate converged statistics for the main quantities of interest. Similar time scales have been used in other DFT/MD simulations (e.g., refs 11 and 19). Of course, calculations of very long time-scale properties such as reaction rates may require additional statistics, but that is not the object of the present paper. For each run, radial distribution functions (RDFs) for all atoms in the cluster were obtained. These used all conformations from the post-thermalization period, and the final RDFs are obtained by averaging over the initial conditions. For the computation of electronic properties (net charges, projected densities of state (DOS), and XANES spectra), we used 36 samples extracted from each DFT/MD trajectory, for a total of 144 samples for each temperature and composition, thus ensuring relatively small error bars. The similarity between these RDFs indicates that our sampling procedure generates an adequate statistical ensemble for the treatment of dynamic disorder, which is the main aim of this paper. The net charges were obtained from a Bader analysis of the VASP electron densities.[20] The projected DOS and XANES

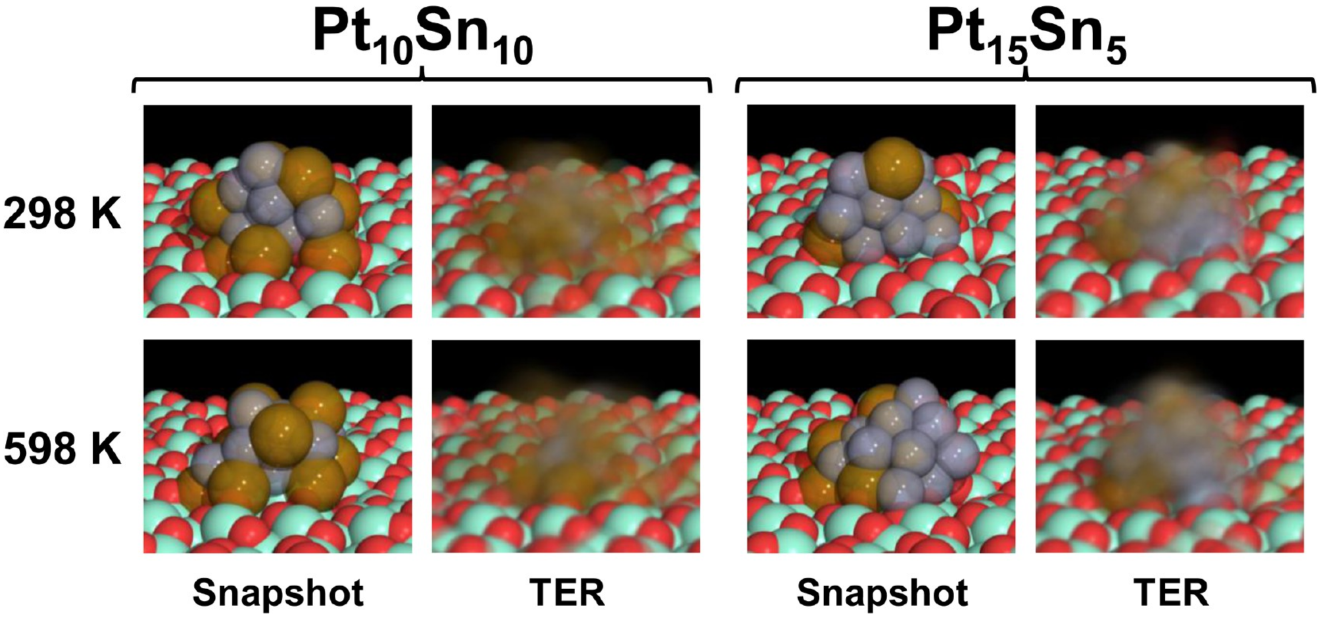

Figure 1. Snapshots of our DFT/MD simulations at $t = 4$ ps for selected trajectories and time-elapsed renderings (TER) at two different compositions and temperatures. The TER images were generated by averaging over all four initial conditions and over the 8 ps of the DFT/MD. Their "fuzziness" characterizes the disorder and mobility of the Pt and Sn in these systems.

spectra were obtained from FEFF9 calculations,[21] using muffin-tin radii of 3.6 Å for the SCF potentials and cluster radii of 8 Å for the full multiple scattering calculations. As shown for example by a previous study of Pt_{10}, the FEFF code yields semiquantitative results for such Pt edges. To improve the relative energy scales between FEFF and VASP at different compositions, we used the correction approach described in detail in ref 22; briefly, the total DOS is computed with both VASP and FEFF, and equivalent features (e.g., sp band, d band, etc.) are aligned. The Fermi energy from FEFF is then shifted to match the more accurate, full-potential VASP values. These corrections are small (0.7 to 1.2 eV), but are critical for obtaining accurate edge shifts and white-line intensities. In addition, to take into account the oxidized and metallic nature of the Pt and Sn atoms, we chose different representative FEFF9 potentials for atoms bound to the support O atoms.

In addition to bare supported clusters, we have also briefly investigated the effects of structural fluctuations and inhomogeneity at elevated temperatures. To achieve a qualitative understanding of the effect of cluster and substrate dynamics on the reactivity of a prototypical molecule (H_2), we have used an approximate method, here dubbed "quasi-instantaneous thermal sampling" (QITS). First, we extract snapshots from our MD simulations at different temperatures and concentrations. Second, we physisorb the molecule of interest with random orientations at random sites on the nanoparticle and then relax the molecule, keeping fixed the internal structure of the support and nanoparticle. Because reactivity occurs in the subpicosecond regime, QITS captures the effects of picosecond scale particle morphological distortions, ignoring subpicosecond local vibrational effects.

■ RESULTS AND DISCUSSION

Nonequilibrium Morphology and Dynamics. Visual inspection of the MD trajectories reveals (see animation in Supporting Information) that the nanoparticle structure is highly fluxional, with dynamical bond breaking and reforming over a time scale of several picoseconds. This effect is similar to that previously observed for supported Pt_{10} nanoclusters.[11] In contrast with Pt_{10}, however, the presence of Sn has profound effects on both cluster structure and properties. Because of their fluctuating structures, the clusters can be characterized as close-packed and semimelted or amorphous. Nevertheless, their gross global structure can be represented as hemispherical. These characteristics are illustrated in the snapshots and time-elapsed (TER) structures in Figure 1. Thus, as a gauge of morphology, we have calculated the average nanoparticle half axial lengths from their instantaneous moments of inertia. These are used to fit the nanoparticles to a hemielliptical shape, with half axial lengths "*a*" and "*b*" approximately parallel and "*c*" approximately perpendicular to the support. The trajectories of these parameters show an initial flattening during thermalization, which, as discussed below, is largely driven by the Coulomb repulsion between the Sn atoms. After thermalization (i.e., after ~3 ps) at RT, the $Pt_{10}Sn_{10}$ clusters are found to have an elongated cross section parallel to the support, with average hemiaxial lengths a and b about 5.8 and 4.2 Å and a height c about 7.6 Å (Supporting Information, Figure S1), although there seems to be nothing special about this asymmetry. This gives (Figure 2, top) an estimated volume ($(2/3)\pi abc$) of 388 $Å^3$ (RT). At high temperature, the particles become slightly flatter and broader, and their volume increases to ~407 $Å^3$, consistent with positive thermal expansion (PTE). The $Pt_{15}Sn_5$ clusters have similar structures except for the marked decrease in cluster height, which lowers the volume to 332 (RT) and 319 $Å^3$ (OT). This trend toward NTE at larger Pt concentrations is consistent with other properties further discussed below.

Figure 2 (bottom) shows a typical trajectory for the CM of $Pt_{10}Sn_{10}$ at different temperatures. The collective motion of the nanoparticles is clearly enhanced at OTs: For $Pt_{10}Sn_{10}$, the mean-square displacement (MSD) of the CM parallel to the surface is 0.03 $Å^2$ at 298 K and roughly doubles to 0.07 $Å^2$ at 598 K. These fluctuations are somewhat smaller than those observed for Pt_{10}, where a parallel MSD of 0.08 $Å^2$ was

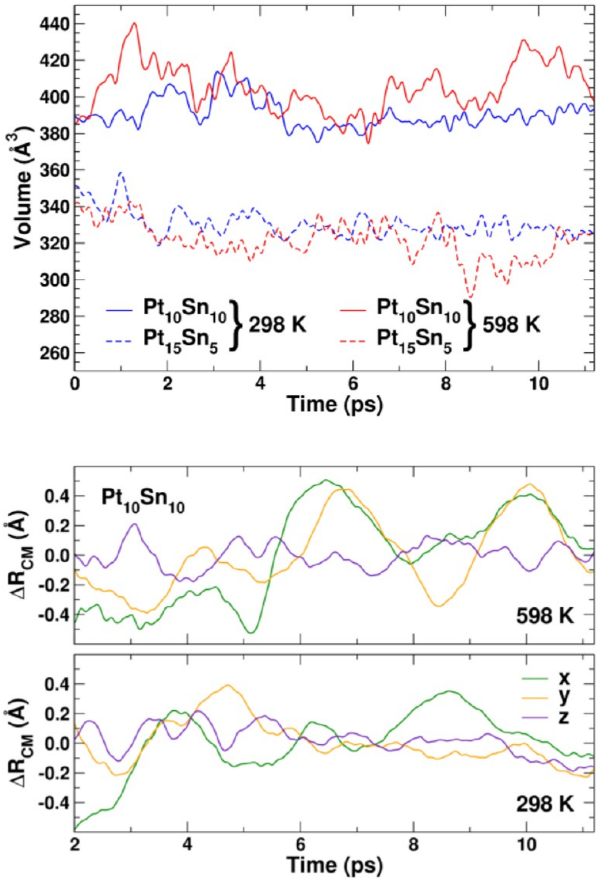

Figure 2. Average nanoparticle volume (top) computed from the moments of inertia by assuming that the nanoparticles have an overall hemielliptical shape and (bottom) center of mass position change for a typical $Pt_{10}Sn_{10}$ trajectory. Note the larger center of mass fluctuations under operando conditions.

observed at 165 K.[11] The difference is likely due to the heavier nature of the present 20 atom clusters and the larger number of support-anchoring bonds. Fluctuations perpendicular to the surface are even smaller, about 0.01 and 0.02 Å^2 at 298 and 598 K, respectively. This suggests that the clusters are more or less anchored to the support (at least over time-scales shorter than ∼10 ps) but can exhibit librational motion with respect to the anchoring pivot point. From statistical mechanics, one expects that an MSD from such 2D motion is proportional to kT/M, and hence Brownian-like, where k is Boltzmann's constant, M is the cluster mass, and T is the absolute temperature.

We also find that composition has a significant effect on the collective motion of the clusters. For $Pt_{15}Sn_5$, the parallel MSD is enhanced to 0.06 and 0.11 Å^2 at 298 and 598 K, respectively. This increase in mobility arises neither from a mass difference (because $Pt_{15}Sn_5$ is 12% heavier than $Pt_{10}Sn_{10}$) nor from a difference in the number of support anchors because it is largely constant. The origin resides in the anchoring, for which $Pt_{10}Sn_{10}$ has a larger number of stronger Sn−O bonds. Figure 2 also reveals the key dynamic time scales in the nanoparticles. The collective motion of the clusters is dominated by "slow" fluctuations of the CM. As noted above, these slow fluctuations can be interpreted largely as librational, with periods roughly 2 to 4 ps (i.e., frequency components 0.2 to 0.5 THz). This is significantly slower than the short-range bond vibrations in metallic Pt, which ranges from 1 to 6 THz. The volume fluctuations also exhibit long period fluctuations (1 to 2 ps or 0.5 to 1 THz), overlaid with fast, small amplitude vibrations. Finally, on even longer time scales (on the order of 10 ps), the CM can exhibit translational motion due to bond breaking with the support, eventually leading to sintering.

Internal Structure of the Nanoparticles. A rough picture of the structure of the nanoparticles is given by their global average properties. These are the quantities directly measured in XAS experiments, but they ignore heterogeneity, which is discussed further below. Figure 3 and Table 1 show, respectively, the average metal−metal RDFs and the average

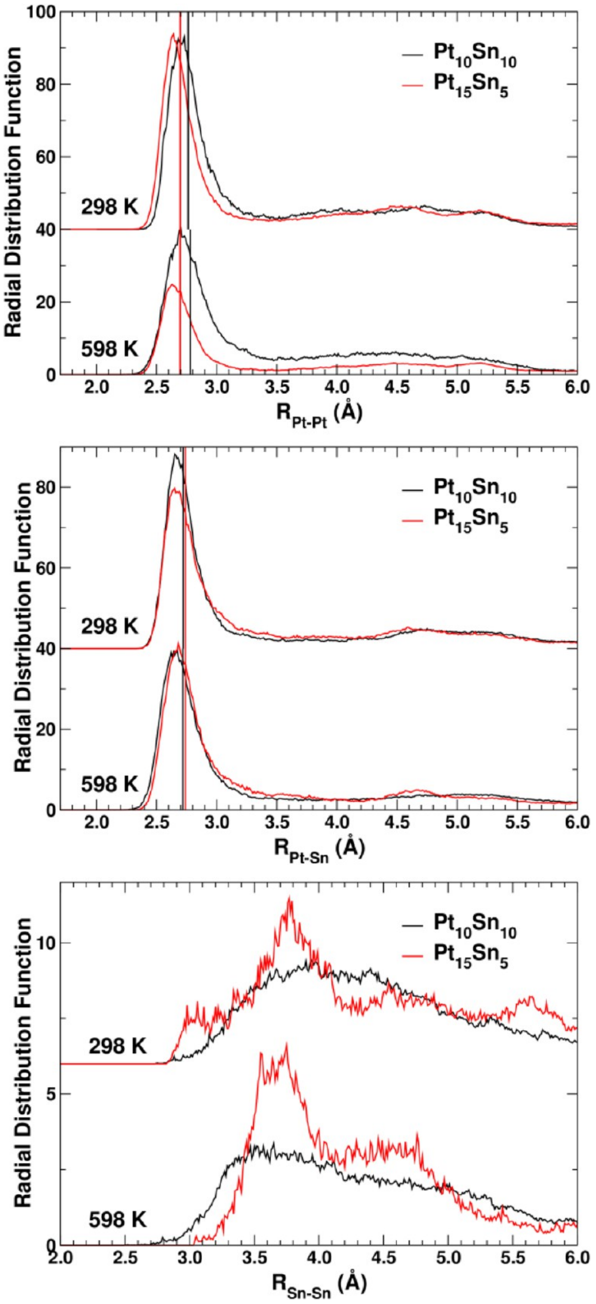

Figure 3. Intracluster radial distributions functions for Pt−Pt (top), Pt−Sn (center), and Sn−Sn (bottom). The vertical lines indicate the centroid of the shell. Note that the first shell of the Pt−Pt RDF is sensitive to both composition and temperature, while that of the Pt−Sn RDF is largely unaffected. The Sn−Sn RDF does not show significant order at high Sn concentrations.

Table 1. Nearest Neighbor Distances and Debye−Waller Factors

		distance (Å)			σ^2 (Å^2)	
		298 K	598 K	Δ	298 K	598 K
$Pt_{10}Sn_{10}$	Pt−Pt	2.762	2.781	0.018	0.023	0.035
	Pt−Sn	2.722	2.718	−0.003	0.018	0.027
	Pt−O	2.127	2.159	0.032	0.007	0.014
	Sn−O	2.211	2.189	−0.022	0.022	0.022
$Pt_{15}Sn_5$	Pt−Pt	2.697	2.696	−0.001	0.019	0.020
	Pt−Sn	2.739	2.739	0.000	0.024	0.026
	Pt−O	2.110	2.157	0.047	0.011	0.017
	Sn−O	2.147	2.171	0.024	0.028	0.029

structural parameters of the Pt−Sn nanoclusters. The vertical lines in the RDFs indicate the average first near-neighbor distances. These RDFs suggest that on average the clusters have fairly well-defined near-neighbor Pt−Pt and Pt−Sn coordination, as shown by the narrow first shell peaks between 2.7 and 2.8 Å. An increase in the Pt concentration leads to a contraction of 0.07 Å in the first Pt−Pt coordination shell and a more ordered system, as shown by the smaller mean-square relative displacements (MSRDs) summarized in Table 1. While the average Pt−Pt distance in $Pt_{10}Sn_{10}$ shows an expansion, the Pt−Pt interaction in $Pt_{15}Sn_5$ shows almost no thermal effect, consistent with the small volume contraction described above. This trend toward NTE at higher Pt concentration is also consistent with our observation of NTE in pure Pt clusters.[11,23]

Global averages, however, can be misleading for characterizing inhomogeneous structures and point to the importance of both theory and experiment to elucidate the properties of these systems. Thus to understand the RDFs in more detail, we show in Figure 4 (top) the first shell region of the Pt−Pt RDF of $Pt_{10}Sn_{10}$ at 298 K, which has been decomposed according to the number of Sn nearest-neighbors. This global average RDF is composed mainly of Pt atoms with two or three Sn neighbors in equal weight. Note that the mean Pt−Pt distances for each population increase monotonically with respect to the number of neighbors (Figure 4, bottom). This suggests a weakening of the Pt−Pt bond or a Coulomb driven stretch in the presence of Sn, consistent with the Pt−Pt contraction in Sn-poor particles. Such correlations are useful in analyzing XAS data.

Remarkably, the first Pt−Sn shell (Figure 3, middle) is largely unaffected by temperature and composition changes. This suggests a possible relation between the two metallic components because temperature increases result in neither bond expansion nor increased disorder. As discussed below, this finding is consistent with the observation that the Sn atoms tend to lie on the surface of the cluster and have a higher mobility on it.

For the Sn−Sn interaction, the $Pt_{10}Sn_{10}$ RDFs at RT and OT show poorly defined shells with onsets at the metallic Sn nearest neighbor distance (~2.8−3.0 Å), and broad peaks between 3.2 and 4.5 Å. At higher %Pt the RDFs reveal emerging peaks at ~3.8 Å, indicating that partial order develops in the Sn−Sn shell. This emerging structure originates from the maximal dispersion of the positively charged Sn atoms on the cluster surface due to their Coulomb repulsion. A rough estimate from the MD simulations gives a distance of ~3.6 Å between maximally separated Sn atoms.

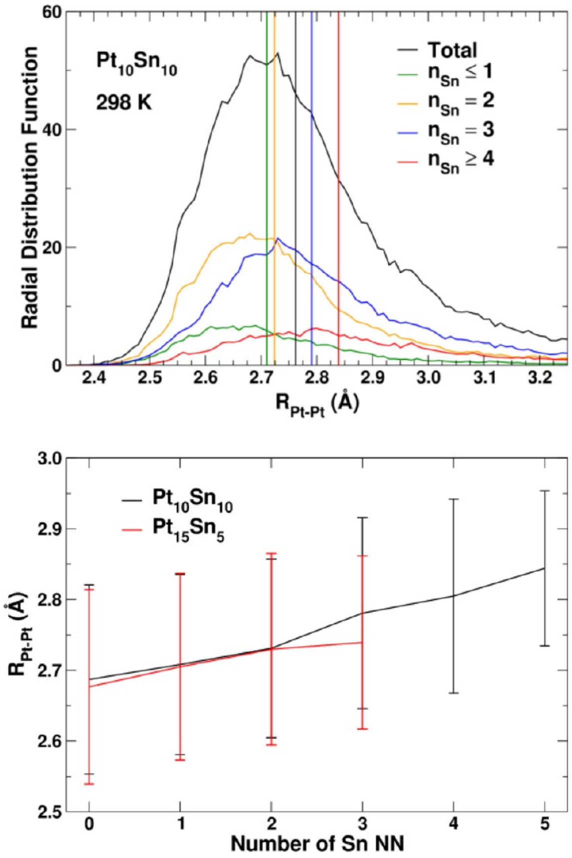

Figure 4. Intracluster Pt−Pt radial distributions function for $Pt_{10}Sn_{10}$ at 298 K, decomposed as a function of number of near-neighbor Sn atoms (top). The vertical lines indicate the centroid of the shell. Average Pt−Pt distance as a function of the number of Sn near-neighbors (bottom), with error bars indicating the standard distribution of the distances. The monotonic increase in the bond distance shows the local weakening effect of Sn alloying.

Table 2. Number of Nearest Neighbors of Type B around Atom Type A and Cowley Short-Range-Order Parameter *a* and Its Surface Component α^S

	298 K		598 K	
n_{AB}	$Pt_{10}Sn_{10}$	$Pt_{15}Sn_5$	$Pt_{10}Sn_{10}$	$Pt_{15}Sn_5$
n_{PtO}	0.2	0.5	0.2	0.4
n_{PtPt}	3.0	4.0	2.6	4.0
n_{PtSn}	2.6	1.2	2.5	1.3
n_{SnO}	1.1	1.0	1.1	0.8
n_{SnPt}	2.6	3.5	2.5	3.7
n_{SnSn}	0.3	0.2	0.5	0.1
α_{Pt}	0.1	0.1	0.0	0.1
α^S_{Pt}	−0.2	0.2	−0.2	0.2
α_{Sn}	−0.8	−0.3	−0.7	−0.3
α^S_{Sn}	−0.8	−0.3	−0.6	−0.2

Table 2 shows the number of nearest neighbors (n_{AB}), as obtained by integrating the area under the first coordination shell. Not surprisingly, the composition has a larger effect on n_{AB} than the change in temperature. Also, an increase in the percentage of Pt increases the average number of Pt−Pt near neighbors. The change is ~33% (about one Pt atom), which is less than the 50% change in Pt concentration. Correspondingly, the number of Sn atoms around each Pt is reduced by about 1.0 and 1.4 Sn atoms at 298 and 598 K, respectively. Overall, the number of neighbors around a given Pt atom remains nearly constant (~5.8), with the excess loss of Sn neighbors counteracted by an increase in the number of O neighbors, as discussed below.

Our DFT/MD calculations for the 20-atom γ-Al_2O_3 supported clusters show that their structures differ markedly from their bulk counterparts. In bulk Pt−Sn alloys the Pt−Sn bond length varies from a crystallographic value of 2.83 Å in Pt_3Sn (which is face-centered cubic with Sn at the corners and Pt on the faces) to 2.73 Å in PtSn (which is hexagonal close-packed with ABAC stacking, Pt in the A layers, and Sn in the B and C layers). Our simulations for the Pt−Sn nanostructures yield a Pt−Sn bond length of 2.72 and 2.74 Å for temperatures 298 and 598 K, in agreement with the bond lengths of the bulk PtSn, and vary little over the 3:1 to 1:1 Pt:Sn composition range. The calculations also show that for $Pt_{10}Sn_{10}$ the average Pt−Pt bond length is shorter than the Pt−Sn bond length, whereas for $Pt_{15}Sn_5$ the order is reversed. As discussed below, we find that this difference is largely due to a change in the Pt charge, while the average charge on the Sn remains relatively constant. In the Sn-rich cluster the Pt is more negatively charged, leading to increased Coulomb repulsion and longer Pt−Pt bond lengths. These new insights may help explain why previously published experimental data from alumina-supported PtSn clusters are mixed in terms of reporting that the Pt−Pt bond length is longer than the Pt−Sn bond length,[5,24,25] or the Pt−Pt bond is shorter than the Pt−Sn bond length[7,26] or indeed whether the bond lengths are equal.[8,27]

The simulations also show that there is significant anomalous nonvibrational disorder in the average Pt−Pt and Pt−Sn bond lengths (Table 1), which we term "dynamic structural disorder" (DSD). This DSD is manifested in the anomalously large average MSRD σ^2 values in these systems. The values for the Pt−Sn clusters are significantly greater than those reported for the Pt-only clusters.[11] The majority of XAFS experimental data report that the σ^2 value for Pt−Sn is larger than that for Pt−Pt in γ-alumina-supported PtSn clusters. In our calculations, this is only the case for Pt-rich clusters, which exemplifies the variation of disorder in these systems.

Dynamic Structural Disorder. It is conventional in XAS analysis to characterize the MSRD in terms of additive vibrational and structural disorder contributions, that is, $\sigma^2 = \sigma^2_{vib} + \sigma^2_{dis}$, with the latter usually regarded as static. However, our DFT/MD simulations show for the Pt−Sn nanoclusters that the structural disorder is largely dynamic in origin. To understand the roles of both structural and vibrational disorder, we have decomposed the dynamics of bound Pt−Pt pairs by applying a $f = 0.5$ THz low-pass filter that separates the slower structural disorder from the faster vibrational components. This filter is carried out using a convolution of the real-time Pt−Pt trajectories with a sine function of length π/f.

Figure 5 (top) shows this decomposition for a typical trajectory for $Pt_{10}Sn_{10}$ at 298 K. The fast vibrational components have periods between 200 and 500 fs, while the dynamical structural disorder has periods between 1 and 4 ps. These time scales can be clearly seen in the average power spectra (Figure 5, bottom), obtained by averaging the Fourier transform of all bound pair Pt−Pt trajectories for $Pt_{10}Sn_{10}$. Both the RT and OT spectra show a vibrational spectral density between about 1 and 5 THz, consistent with the phonon vibrational spectrum in metallic Pt. The DSD appears at lower frequencies between 0.1 and 0.6 THz. The thermal effects on the two components are also different. The vibrational component shows a linear increase in the MSRD with increasing temperature, consistent with the statistical mechanics of harmonic oscillators, with little change in the frequency distribution. In contrast, the DSD has a smaller, albeit non-negligible variation with temperature. This separation can also be used to analyze the MSRDs for the vibrational and structural disorder components: for $Pt_{10}Sn_{10}$, the vibrational σ^2_{vib} is 0.010 Å^2 at 298 K and 0.020 Å^2 at 598 K, while the structural disorder component σ^2_{dis} is 0.014 Å^2 at 298 K and 0.018 Å^2 at 598 K. The origin of the DSD appears to be correlated with the librational motion of the CM but may also include noninertial effects and stochastic changes in the local environment due to fluctuating internal motion. Finally, given that only bound pairs were used in this analysis, these results do not capture the transient time scale at even lower frequency associated with Pt−Pt pair breaking, which accounts for events that occur once or twice per 10 ps trajectory for about a third of the pairs.

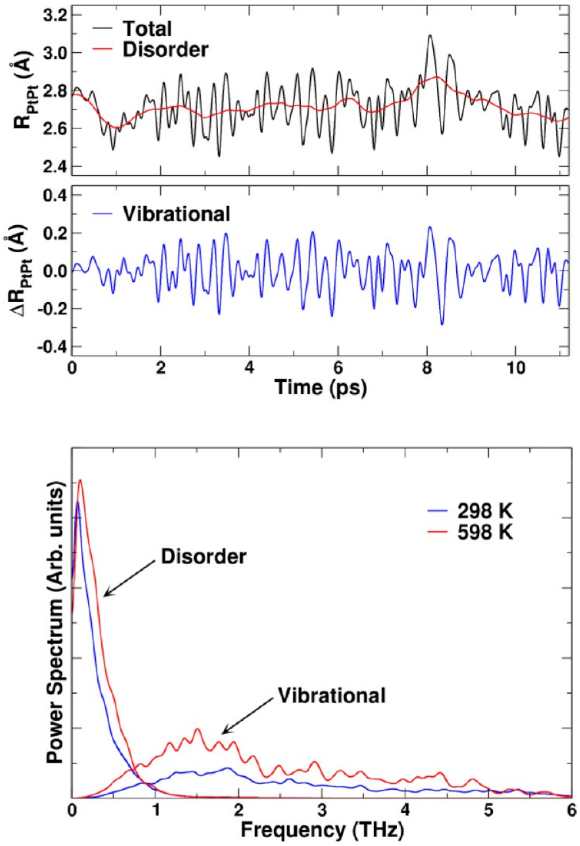

Figure 5. Typical total trajectory for a bound Pt−Pt pair in $Pt_{10}Sn_{10}$ at 298 K decomposed into structural disorder and vibrational components by applying a 0.5 THz low-pass filter (top) and average power spectrum for the vibrational and dynamic structural disorder components of bound Pt−Pt pairs in $Pt_{10}Sn_{10}$ as a function of temperature (bottom).

Short-Range Order. To further explore the near-neighbor ordering between the Pt and Sn in the clusters, we have calculated the Cowley short-range order (SRO) parameter $\alpha_A = 1 - n_{AB}/n_{AM}\, x_B$, where n_{AB} is the number of atoms of type B around an atom of type A, $n_{AM} = n_{AA} + n_{AB}$ is the total number of atoms of type A or B around an atom of type A, and x_B is the fraction of atoms of type B in the cluster.[28,29] Positive values of α_A correspond to positive clustering, that is, a preference for atoms of the same type as near-neighbors; negative values to a preference for atoms of a different type; and values near zero to random near-neighbor type distributions. Thus, for large core−shell particles with negligible interface volume, α_A is positive for both components. For small nanoparticles, however, where the interface between the core and shell is a substantial part of the total particle volume, the relation between the short-order parameter and the particle structure should be carefully analyzed. Table 2 shows that α_{Sn} is negative in all cases, implying that the Sn atoms have a tendency to be surrounded by Pt and segregated from other Sn atoms. This is also clear from n_{SnSn}, which shows little or no affinity between the Sn atoms. The increase in α_{Sn} for Pt-rich clusters is due purely to the change in the cluster's Sn fraction.

For Pt, we find that α_{Pt} averaged over the entire cluster is nearly zero or slightly positive. In large particles, this would indicate random SRO. However, a closer analysis that takes into account inhomogeneity shows that the average value arises from positive and negative clustering from populations of interior and surface Pt atoms. This is shown in Figure 6 (top), where α_{Pt} is plotted as a function of the distance to the center of the cluster (R_{CC}). The surface SRO parameters $\alpha_{\mathrm{Pt}}^{\mathrm{S}}$ and $\alpha_{\mathrm{Sn}}^{\mathrm{S}}$ are defined as the average for those Pt atoms with R_{CC} larger than 4 Å. While α_{Sn} (R_{CC}) is always negative, α_{Pt} (R_{CC}) varies from positive clustering near the center to negative at the surface. The surface values in Table 2 also display this trend toward negative clustering for $Pt_{10}Sn_{10}$. For $Pt_{15}Sn_5$, the Sn concentration is too low to generate negative clustering, and hence positive clustering dominates. The hallmark of core–shell segregation can also been seen in the change of near-neighbor distribution from Pt-rich to Sn-rich for a probe Pt atom, shown in Figure 6 (bottom). These results clearly illustrate the effect of the segregation of the Sn atoms to the cluster surface and the large differences between surface and internal structure.

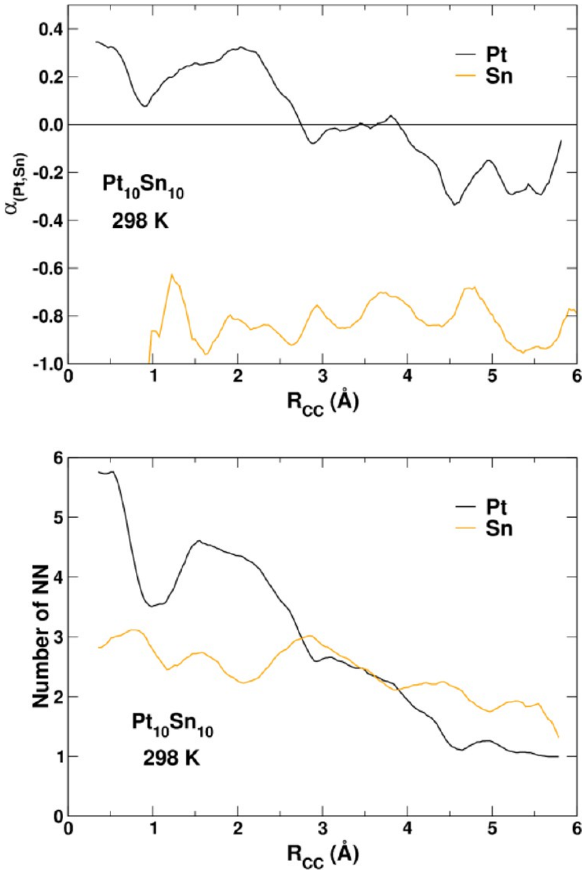

Figure 6. Cowley short-range-order parameter α (top) and number of Pt and Sn nearest neighbors around a Pt atom (bottom) as a function of distance to the cluster center for $Pt_{10}Sn_{10}$ at 298 K. While the Sn order parameter shows negative clustering going from cluster center to surface, for Pt, the parameter changes from positive to negative clustering at ~3.5 Å. This transition from the Pt core to the Sn shell is strongly correlated with the number of nearest neighbors.

Nanoparticle–Support Interactions. Comparing Pt–Sn clusters, the most noticeable effects on the average cluster–support interactions arise from changes in composition rather than temperature. In particular, the effective contact between the Pt atoms and the support decreases with increasing Sn concentration (Figure 7). This is seen in both the average Pt–O distance, which increases from 2.11 Å in $Pt_{15}Sn_5$ to 2.13 Å in $Pt_{10}Sn_{10}$, and the number of O neighbors per Pt atom, which drops from 0.5 to 0.2. This change in the nature of the cluster–support interaction with composition can be seen in Figure 8, which shows the atomic distribution perpendicular to the support, that is, the "z" distribution function (zDF). The support surface ($z = 0$) is defined by the mean position of the topmost layer of O atoms, that is, the centroid of the O zDF (red curves). For $Pt_{10}Sn_{10}$, the nearest neighbor region (at about 1.5 to 2.5 Å above the support) is rich in Sn atoms and poor in Pt atoms. In $Pt_{15}Sn_5$, the situation is reversed, with more Pt atoms near the support.

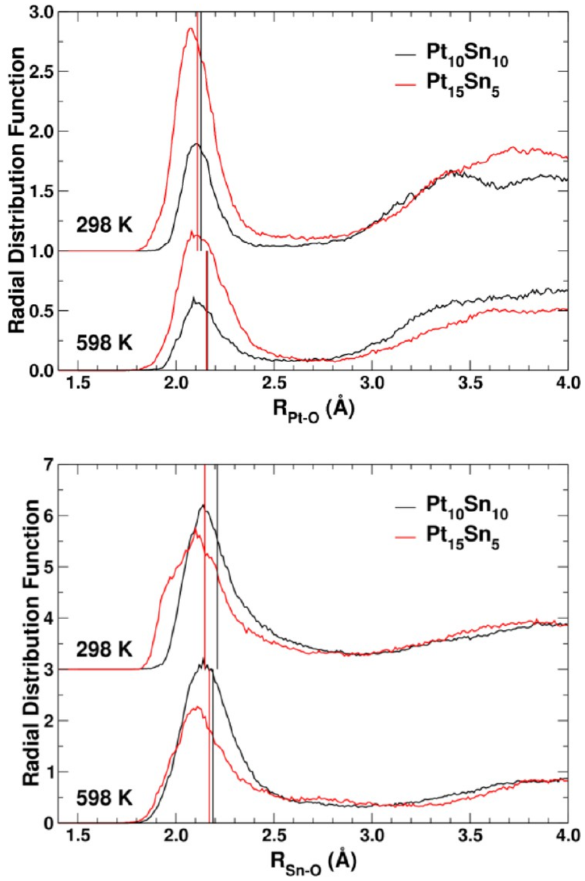

Figure 7. Cluster-support radial distribution functions for: Pt–O (top) and Sn–O (bottom). Note the substantial decrease in cluster–support interaction with increasing Sn concentration. The data for 298 K are offset vertically for clarity.

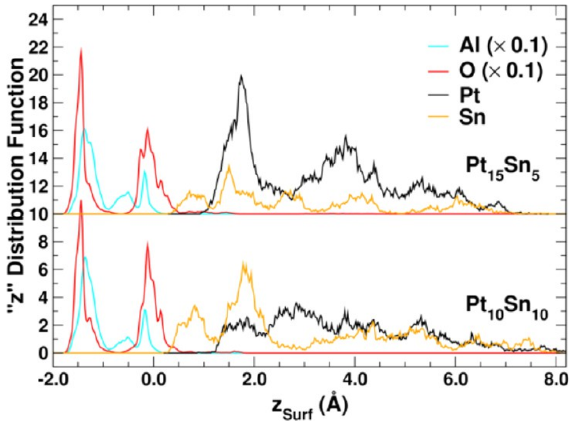

Figure 8. Distance distribution functions (zDF) orthogonal to the support surface for $Pt_{10}Sn_{10}$ and $Pt_{15}Sn_5$ at 298 K. Note the preferential embedding of Sn on the substrate for $z < 1.5$ Å. On average, half of the Sn atoms are in contact with the support ($z < 2.5$ Å). The data for $Pt_{15}Sn_5$ are offset for clarity.

In contrast, the number of O atoms per Sn (about one) remains mostly constant, indicating that the interaction between the Sn and the support is roughly independent of temperature and concentration. However, this result does not imply that all Sn atoms are in contact with the support because the number of O atoms per Sn atom is the average of two distinct populations: one associated with the surface of the cluster (with $n_{SnO} = 0$) and another associated mostly with the rim of the cluster along the support (with $n_{SnO} \geq 1$). This latter population has such a strong interaction with the O atoms that some Sn atoms lie very close (<1.5 Å) to the support surface, as in Figure 8. Given that the Sn−O distance is always longer than 1.9 Å, this indicates a tendency to embed into the support and form SnO_2-like moieties. The Pt atoms show little tendency to embed, always lying 1.5 Å above the support.

The global average DFT/MD values for the Pt−O and Sn−O bond lengths of 2.1 and 2.2 Å, respectively can be directly compared with experiment: In EXAFS analysis of reduced Pt clusters on γ-Al_2O_3, it has repeatedly been found that the mean Pt−O bond length is in the range of 2.1 to 2.2 Å; this has been interpreted as the Pt−O bond between the Pt atoms on the surface of the cluster and the alumina surface.[30−32] For comparison, the Pt−O bond in bulk PtO_2 is 2.07 Å. For Sn, the Sn−O bond length in SnO is 2.22 Å, and in SnO_2 it is 2.05 Å. Our calculated values of the Sn−O bond length supports the conclusion that the Sn in direct contact with the alumina support is positively charged, with a value close to two (see below).

Electronic Structure. The electronic structure and charge distribution within the nanoparticles is of particular interest because they are determining factors in their catalytic activity. One way to characterize this behavior is via the partial or net atomic charge on each atom in the cluster. These charges can be estimated from a Bader analysis, where the charge is defined as the excess or deficiency of charge with respect to the neutral atom (see, for example, ref 11).

Figure 9 shows the charge distribution as a function of the distance z above the support surface for both species in $Pt_{10}Sn_{10}$ and $Pt_{15}Sn_5$. The individual symbols represent the net charges of each individual atom, sampled from MD snapshots. The average charges, indicated by the horizontal dashed lines and the scale on the right of the plots, show that the Sn atoms have about one unit of positive charge that is largely unaffected by composition (+0.94e in $Pt_{10}Sn_{10}$ vs +1.06e in $Pt_{15}Sn_5$). The Pt atoms are negatively charged in $Pt_{10}Sn_{10}$ (−0.49e) and nearly neutral in $Pt_{15}Sn_5$ (−0.11e). From the average charges and cluster compositions, we obtain the total cluster charges $Q_T = Q_{Pt}^{Avg} n_{Pt} + Q_{Sn}^{Avg} n_{Sn}$, where n_X is the number of atoms of type X and Q_X^{Avg} is their average charge. Thus the clusters are, on average, positively charged, as expected given the electronegativity of the O atoms on the support. Moreover, Sn-rich clusters are slightly more positively charged (+4.5e) than Sn-poor ones (+3.7e). We also note that there are substantial charge fluctuations about these mean values due to the transient bonding of the cluster to the alumina support.

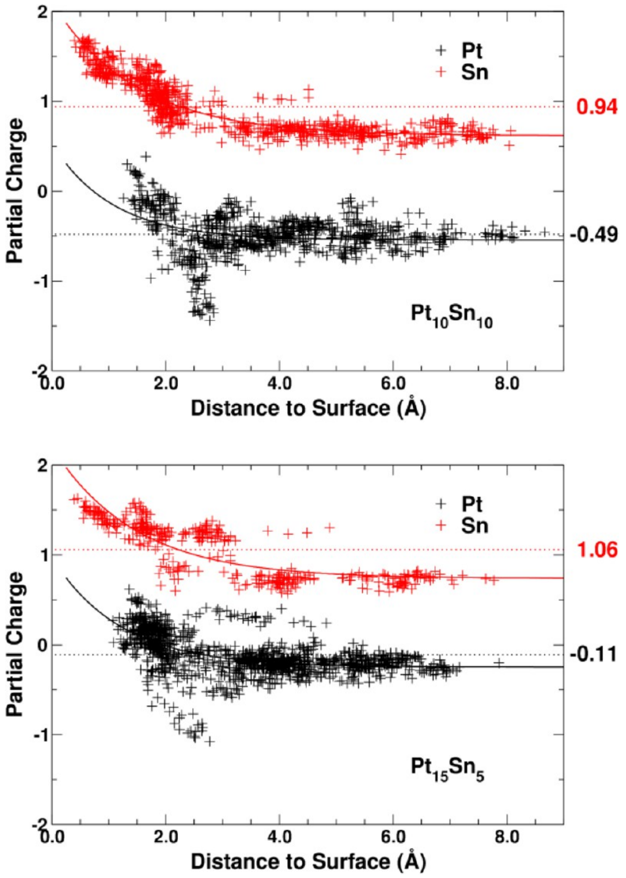

Figure 9. Net atomic charge of the Pt and Sn atoms in $Pt_{10}Sn_{10}$ (top) and $Pt_{15}Sn_5$ (bottom) at 298 K. The dashed lines indicate the average charge for each species, also indicated by the numbers on the right-hand side of each plot. The full lines correspond to a fit to a simple overlap charge-transfer model $Q = Q_\infty + e^{(-\lambda z)}/\lambda$ model, where Q is the net charge, z is the distance to the support surface, Q_∞ is the charge at infinite separation, and λ is the charge density distribution parameter.

In addition, the "z" profiles in Figure 9 show that the charge distribution is more-or-less homogeneous above a substrate dominated "O-interaction" region that extends up to ~2.5 Å. As shown in Figure 7, the 2.5 Å boundary agrees with the upper limit of both the Pt−O and Sn−O interactions. The net atomic charges Q can be fit with a simple model $Q = Q_\infty + e^{(-\lambda z)}/\lambda$ that takes into account the overlap charge transfer. Here z is the distance to the support surface, Q_∞ is the net charge at infinite separation, and λ is the charge-density distribution parameter. Extrapolating this model (full lines in Figure 9). we can estimate the limiting (Pt,Sn) charges to (−0.6e,+0.6e) for

$Pt_{10}Sn_{10}$ and (−0.3e,+0.9e) for $Pt_{15}Sn_5$. Thus, taking into consideration the composition ratios of 1:1 and 3:1, the clusters approach stoichiometric neutrality away from the support. In the O-interacting region, the charges are more positive due to electron-withdrawing by the O atoms. These charge distributions can help explain some interesting properties observed in the RDFs: First, the net positive charges of the Sn lead to large Coulomb repulsion and minimal interaction between them, resulting in the lack of structure in the Sn−Sn RDF. Second, the affinity between the Sn atoms and both the Pt atoms and the support appears to be partially due to Coulomb attraction between the oppositely charged species. Moreover, the increase in the support-affinity of the Pt atoms in the Sn-poor clusters probably results from their less negative overall charge. Finally, this change in the Pt charge is likely associated with the 0.07 Å contraction in the Pt−Pt shell. Overall, these properties are consistent with a simple electrostatic picture with a core predominantly formed from relatively neutral Pt atoms and an outer shell of positive, mutually repelling Sn atoms.

Our results are consistent with prior experimental work where the presence of oxidic tin has been noted, especially those using an alumina support. For example Meitzner et al.[6] postulated that the form of the PtSn clusters consisted of platinum clusters dispersed on the alumina that has Sn^{2+} present at the surface, Burch concluded that the Sn is stabilized in the Sn(II) state by interaction with the support,[33] and more recently Iglesias-Juez et al.[8] concluded that the Sn atoms are preferentially located at the surface of the Pt nanoparticles and are present as SnO. In contrast, our study shows that little of the Sn in these clusters is in the form of SnO.

The average local d density of states (dDOS) for Pt, shown in Figure 10, highlights another aspect of the electronic structure, which is important for interpreting the white line and onset of the XAS (see also Supporting Information Figure S2). Overall, the dDOSs for the Pt−Sn systems are similar and show that the clusters are metallic in character with a large dDOS at the Fermi energy. Significant differences exist near the Fermi energy, where the DOS of Sn-poor clusters is larger, and near the center of the d band, where it is depleted. Thermal effects are small, mostly consisting of an enhancement at the band center. Figure 10 (top) also shows a shift to lower energies in the d band center of the alloy nanoparticles with respect to the unalloyed Pt_{10} clusters.

Figure 10 (bottom) shows the unoccupied dDOS in the XANES region. The change in dDOS at the Fermi energy (or threshold for XAS) can also be observed in the simulated Pt L_3 edge XANES spectra shown in Figure 11 (top), where the white line is less intense in Sn-rich clusters. This reduction is consistent with experimental observations that the Pt L_3 white line decreases on addition of Sn, which is due to the net charge transfer from Sn to Pt.[6,7,10,25,34] Compared with Pt-only catalysts, there is also a notable blue shift in the edge position in PtSn catalysts roughly consistent with recent observations of +0.3[34] or +0.6 eV.[10] Another noticeable difference occurs in the EXAFS region (11 600 eV), where there is a significant phase shift between the two compositions, as seen in the $I_{Pt_{15}Sn_5} - I_{Pt_{10}Sn_{10}}$ difference (inset in Figure 11, top). This shift is largely due to the 0.07 Å contraction in the first Pt−Pt coordination shell (i.e., the dominant scattering path). Figure 11 (bottom) shows the Sn K-edge XANES spectra, which display only small changes in the XAS threshold and white line intensity. There is little variation in the EXAFS region, however, in agreement with the relative insensitivity of the Sn environment as a function of composition (Figure 3, bottom).

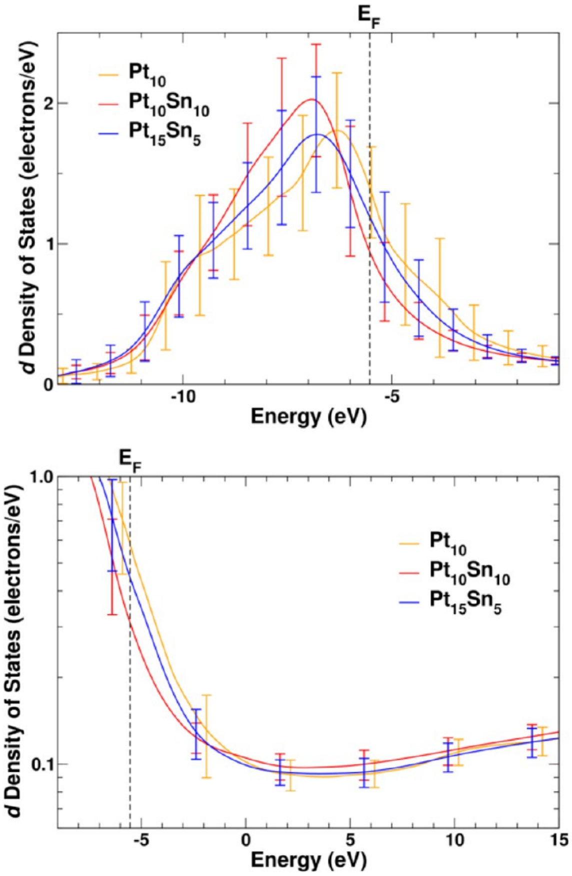

Figure 10. Average Pt local *d* density of states (dDOS) at 298 K as a function of composition for occupied (top) and unoccupied (bottom) states. The vertical dashed line indicates the position of the Fermi level. The error bars represent the mean variation due to dynamics.

Adsorption and Dissociation of H_2. In a preliminary attempt to investigate the role of temperature and dynamical disorder on the reactivity of the nanoparticles, we have used our QITS analysis to study the probability distributions for inter- and intramolecular distances and angles and their correlation. Although this limited study is not intended to be representative of operando conditions, it yields results that may be useful in more detailed future investigations. As a rough gauge of the reactivity of the clusters with adsorbed hydrogen, Figure 12 (top) shows that the molecule−particle distances are distributed between 2.3 and 4.3 Å. Within this broad distribution however, two distances, corresponding to chemisorbed (2.4 Å) and physisorbed (2.8 Å) interactions, are clearly favored. Also, as seen in Figure 12 (bottom), the H_2 molecules have a clear preference for parallel or perpendicular orientations relative to the surface of the nanoparticle.

Next, as shown in Figure 13 (top), the mean H−H distance has a bimodal distribution, with short (0.752 Å) and long (0.764 Å) bond species. The short-bonded species, with a distance close to the unperturbed molecule, are associated with the physisorbed interaction with the particle (2.8 Å), while the long-bonded ones correspond to chemisorption (2.4 Å). This correlation is seen in Figure 13 (bottom). Three regimes can be distinguished: (1) above about 2.7 Å, the H−H distance remains close to the unperturbed distance; (2) between about 2.3 and 2.7 Å, the H−H distance increases to the observed

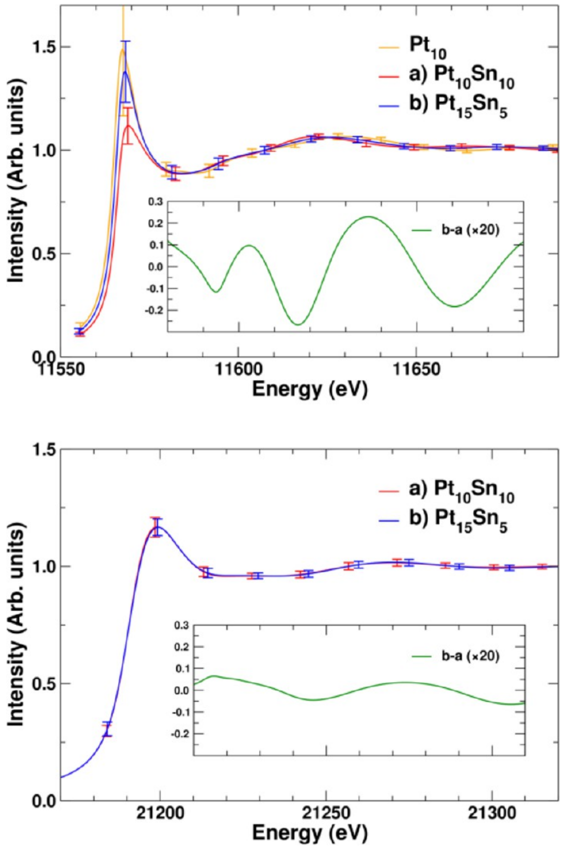

Figure 11. Theoretical XANES spectra of PtSn nanoparticles and Pt_{10} on γ-Al_2O_3 at 298 K for the Pt L3 edge (top) and the Sn K edge (bottom). For comparison, the difference in intensities $I_{\mathrm{Pt_{15}Sn_5}} - I_{\mathrm{Pt_{10}Sn_{10}}}$ in the EXAFS region is also included in the insets, showing the phase shift induced by the contraction of the Pt−Pt bonds. As observed in experiments, the spectra show a lower white line for Sn-rich clusters and a shift to higher edge energies upon Sn alloying.

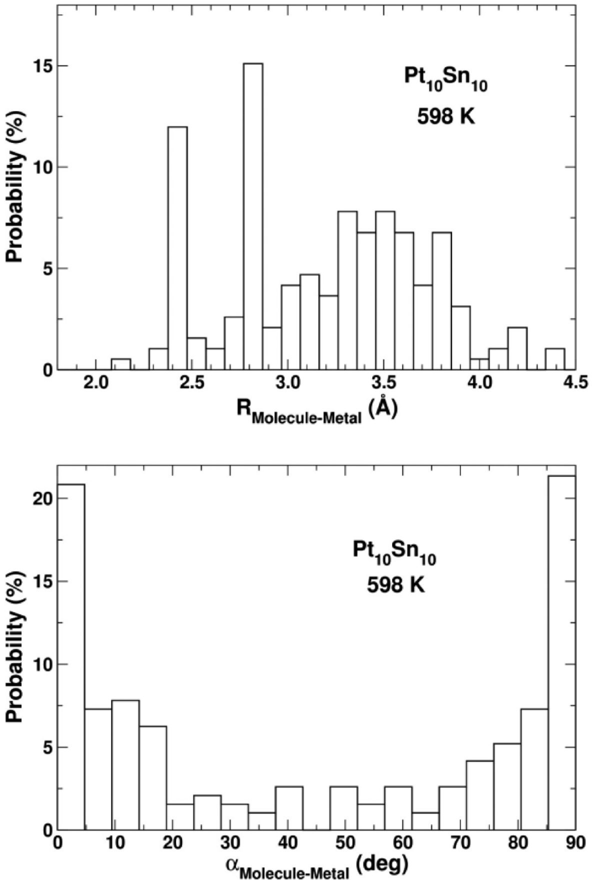

Figure 12. Probability distributions for the molecule-metal distance (top) and angle (bottom) as a function of composition and temperature for the adsorption of H_2 on PtSn nanoparticles. (See Figure S3 in the Supporting Information for other compositions and temperatures.)

chemisorbed value of about 0.76 Å; and (3) below about 2.3 Å (the substrate interaction region), the molecules are either pre- or fully dissociated. QITS predicts that molecules have low (<1%) probability to dissociate on the $Pt_{10}Sn_{10}$ particles at either 298 or 598 K. On $Pt_{15}Sn_5$, however, the probability increases to 5% at 298K and doubles to ∼10% at 598K.

Implications for Catalysis. The picture that emerges from our finite temperature DFT/MD simulations is that of Pt−Sn clusters, in which the Sn atoms are positively charged and hence preferentially segregated to the cluster surface. Moreover, the Sn atoms are not tightly bound to a particular site but exhibit fluctuating bonding on a time scale of a few picoseconds, leading to a quasi-liquid-like surface mobility. This implies that the Pt−Sn clusters are neither chemically nor compositionally uniform, hence very different from their bulk or zero-temperature compositions. Because of the importance of the particle surface for catalytic behavior, their surface structure and dynamics are likely to be more important than their global average morphology. In particular, the substantial nonequilibrium dynamic structure exhibited by these nanoclusters leads to a much larger statistical ensemble of configurations.

Because of the surface sensitivity of catalytic reactions of adsorbed molecules, these characteristics have important implications for the catalytic properties of these supported metallic nanoclusters. Although our study is carried out on bare (or nearly so) Pt−Sn clusters, similar fluctuations are expected even in the presence of more substantial reactant coverage. They particularly show the importance of modeling reactivity based on the fluctuating, operando surface characteristics rather than the average composition or static methods based on Boltzmann distributions of equilibrium configurations. Their structural behavior is strongly influenced by both the positively charged Sn and the fluctuating charge transfer to the support. Moreover, it is important to think about a catalyst as a dynamically fluctuating object rather than a static one. Many studies have claimed to study the active catalyst, but the characterization is usually performed at RT, or even lower, and a static description of the local structure is provided. While these studies provide insight and understanding, the actual catalytically active site is only formed under reaction conditions in the presence of the reactants, products, and at the relevant temperature and pressure (chemical potential). Another consequence of such DSD is the presence of fluctuating reaction barriers, which can have substantial effects on reaction rates.

The detailed dynamical structural and chemical information provided by these DFT/MD studies sheds new light on the old concepts of the “ensemble effect”, where the addition of tin dilutes the contiguous ensembles of platinum atoms, the “electronic effect”, where there is charge transfer from the tin to the platinum, and the concept of “Pt−Sn association”. The data

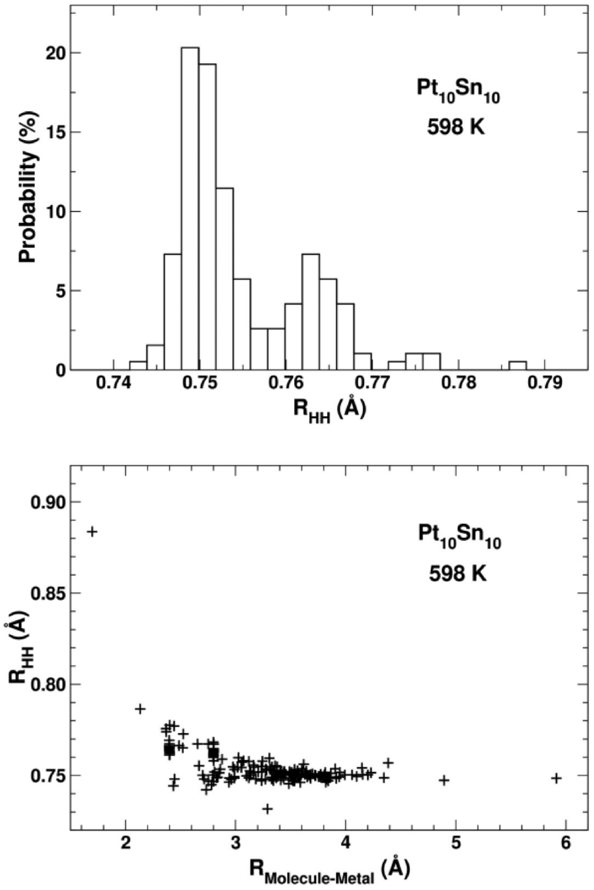

Figure 13. Probability distribution for the H−H distance (top) and correlation between the H−H distance and molecule−metal distance (bottom) as a function of composition and temperature for the adsorption of H_2 on PtSn nanoparticles. (See Figure S3 in the Supporting Information for other compositions and temperatures.)

show that these effects are not static but fluctuate with time and temperature and are strongly influenced by the degree of interaction with the alumina support. The resulting catalytic activity is therefore strongly influenced by all of these parameters, as exemplified by the large difference in the ability of the two clusters studied to dissociate hydrogen, a simple, prototypical reaction, consistent with the concept of Sn attenuation of the dehydrogenation activity of the Pt nanoparticles. It is frequently mentioned in the literature that the addition of Sn stabilizes the Pt clusters against sintering.[8,10,35,36] Our calculations explicitly provide a rationale for this observation − that the clusters are more of less anchored to the support through the strong interaction of the Sn with the alumina surface, particularly around the surface rim of the clusters.

■ CONCLUSIONS

Our combined study of morphology, internal structure, surface interaction, and electronic structure, as calculated by DFT/MD and XAS, gives unique insights into the fundamental driving forces in (20 atom) γ-alumina-supported PtSn nanoclusters at room and operando temperatures. The picture that emerges is that of an inhomogeneous, dynamically fluctuating structure that cannot be fully understood from either a global average perspective or a bulk crystal model. The nanoparticles can be characterized as globally amorphous or semimelted, with internal motion that contains both vibrational and "DSD", the latter of which is large and Brownian-like in nanostructures. On average, they have a roughly hemispherical global shape which for the Sn-rich clusters becomes flatter and broader at OT as compared with RT, consistent with PTE. Sn-poor clusters, however, exhibit a trend toward NTE similar to that in pure Pt$_{10}$ nanoclusters. The particles exhibit large fluctuations in morphology over several time scales, which explains the anomalously large MSRD values observed for these systems. Besides fast near-neighbor vibrations, there is substantial DSD over a time scale of 1−4 ps, driven by the large librational and stochastic motion of the CM. Finally, there is transient, fluxional bond breaking at longer time scales above ~10 ps, with the bond breaking at the support eventually leading to sintering. Notably, the clusters display core−shell segregation. The Pt/Sn distribution within the clusters can be characterized by the short-range-order Cowley parameter, which has a strong temperature and position dependence. Our analysis shows that the Sn atoms are located preferentially at the cluster surface and tend to have Pt neighbors, while the Pt atoms are more randomly distributed. The overall morphology of the clusters can be roughly explained by their internal charge distribution: the net cluster charge is positive due to the interaction with O atoms in the support, with the Sn atoms positively charged and the Pt either weakly negative or neutral. The core−shell segregation is thus driven by Coulomb attraction between the Pt and Sn atoms and repulsion between the Sn atoms that preferentially repels them to the cluster surface.

Given these striking, nonequilibrium behavior and dynamic effects, it is important that the interpretation of global probes like XAS takes into account the differences between surface and internal structure. In particular, EXAFS analysis should take into consideration the qualitative differences between traditional static disorder and dynamical structural disorder and the correlations observed between Pt−Pt and Pt−Sn bond lengths, coordination numbers and position within the cluster. Our electronic structure calculations (using FEFF or VASP) combined with DFT/MD simulations of structure provide detailed local information about overall electronic, thermal, and charge-transfer properties, quantities which affect the edge position and white-line in XAS investigations. For example, the density of states (DOS) is dominated by a large d-electron contribution that is significantly different near the Fermi energy for the different compositions. Although the XAS for these clusters exhibits large dynamic fluctuations, the averages are found to be consistent with the variations in white line intensities and edge positions observed in the literature. The atomistic nature of this information thus permits a deeper and more quantitative understanding of the experimental observations.

■ ASSOCIATED CONTENT

Ⓢ Supporting Information

Animation of typical molecular dynamics trajectories for different compositions and temperatures and more detailed information for nonequilibrium morphology and dynamics, total density of states and adsorption, and dissociation of H_2. This material is available free of charge via the Internet at http://pubs.acs.org.

■ AUTHOR INFORMATION

Corresponding Author

*E-mail: jjr@uw.edu.

Funding

This work was supported by NSF Grant PHY-0835543 (F.D.V., J.J.R.) with computer support from DOE-NERSC and by UOP LLC, a Honeywell Company (S.D.K., S.R.B.).

Notes

The authors declare no competing financial interest.

ACKNOWLEDGMENTS

The authors thank A. Frenkel, K. Asakura, and J. J. Kas for helpful discussions and insights.

ABBREVIATIONS

XAS, X-ray absorption spectroscopy; XAFS, X-ray absorption fine structure; EXAFS, extended XAFS; XANES, X-ray absorption near-edge structure; DFT, density functional theory; MD, molecular dynamics; RDF, radial distribution function; zDF, z distribution function; PTE, positive thermal expansion; NTE, negative thermal expansion; RT, room temperature; OT, operando temperature; DOS, density of states; dDOS, local d DOS; SCF, self-consistent field; MSD, mean-square displacement; MSRD, mean-square relative displacements; DSD, dynamic structural disorder; SRO, short-range order; CM, center of mass; QITS, quasi-instantaneous thermal sampling; TER, time-elapsed rendering; PBE, Perdew−Burke−Ernzerhof

REFERENCES

(1) Sinfelt, J. H. *Bimetallic Catalysts*; Wiley: New York, 1983.

(2) Davis, B. H.; Antos, G. J. In *Catalytic Naphtha Reforming*, 2nd ed.; Antos, G. J., Aitani, A. M., Parera, J. M., Eds.; Decker: New York, 2004; Vol. *61*, p 199.

(3) Li, Y.-X.; Klabunde, K. J.; Davis, B. H. *J. Catal.* **1991**, *128*, 1.

(4) Srinivasan, R.; Davis, B. H. *Platinum Met. Rev.* **1992**, *36*, 151.

(5) Siri, G. J.; Ramallo-López, J. M.; Casella, M. L.; Fierro, J. L. G.; Requejo, F. G.; Ferretti, O. A. *Appl. Catal., A* **2005**, *278*, 239.

(6) Meitzner, G.; Via, G. H.; Lytle, F. W.; Fung, S. C.; Sinfelt, J. H. *J. Phys. Chem.* **1988**, *92*, 2925.

(7) Caballero, A.; Dexpert, H.; Didillon, B.; LePeltier, F.; Clause, O.; Lynch, J. *J. Phys. Chem.* **1993**, *97*, 11283.

(8) Iglesias-Juez, A.; Beale, A. M.; Maaijen, K.; Weng, T. C.; Glatzel, P.; Weckhuysen, B. M. *J. Catal.* **2010**, *276*, 268.

(9) Bazin, D.; Sayers, D.; Rehr, J. J.; Mottet, C. *J. Phys. Chem. B* **1997**, *101*, 5332.

(10) Jahel, A. N.; Moizan-Baslé, V.; Chizallet, C.; Raybaud, P.; Olivier-Fourcade, J.; Jumas, J.-C.; Avenier, P.; Lacombe, S. *J. Phys. Chem. C* **2012**, *116*, 10073.

(11) Vila, F. D.; Rehr, J. J.; Kas, J.; Nuzzo, R. G.; Frenkel, A. I. *Phys. Rev. B* **2008**, *78*, 121404.

(12) Bare, S. R.; Kelly, S. D.; Vila, F. D.; Boldingh, E.; Karapetrova, E.; Kas, J.; Mickelson, G. E.; Modica, F. S.; Yang, N.; Rehr, J. J. *J. Phys. Chem. C* **2011**, *115*, 5740.

(13) Kresse, G.; Furthmüller, J. *Phys. Rev. B* **1996**, *54*, 11169.

(14) Hansen, M. *Constitution of Binary Alloys*; McGraw-Hill: New York, 1958.

(15) Bradley, S.; Sinkler, W.; Blom, D.; Bigelow, W.; Voyles, P.; Allard, L. *Catal. Lett.* **2012**, *142*, 176.

(16) Gjervan, T.; Prestvik, R.; Tøtdal, B.; Lyman, C. E.; Holmen, A. *Catal. Today* **2001**, *65*, 163.

(17) Knözinger, H.; Ratnasamy, P. *Catal. Rev. Sci. Eng.* **1978**, *17*, 31.

(18) Mager-Maury, C.; Chizallet, C.; Sautet, P.; Raybaud, P. *ACS Catal.* **2012**, *2*, 1346.

(19) Yancey, D. F.; Chill, S. T.; Zhang, L.; Frenkel, A. I.; Henkelman, G.; Crooks, R. M. *Chem. Sci.* **2013**, DOI: 10.1039/C3SC50614B.

(20) Henkelman, G.; Arnaldsson, A.; Jonsson, H. *Comput. Mater. Sci.* **2006**, *36*, 254.

(21) Rehr, J. J.; Kas, J. J.; Prange, M. P.; Sorini, A. P.; Takimoto, Y.; Vila, F. *C. R. Phys.* **2009**, *10*, 548.

(22) Vila, F. D.; Jach, T.; Elam, W. T.; Rehr, J. J.; Denlinger, J. D. *J. Phys. Chem. A* **2011**, *115*, 3243.

(23) Kang, J. H.; Menard, L. D.; Nuzzo, R. G.; Frenkel, A. I. *J. Am. Chem. Soc.* **2006**, *128*, 12068.

(24) El Abed, A.; Qebbaj, S. E.; Guerin, M.; Kappenstein, C.; Dexpert, H.; Villain, F. *J. Chim. Phys.* **1997**, *94*, 54.

(25) Uemura, Y.; Inada, Y.; Bando, K. K.; Sasaki, T.; Kamiuchi, N.; Eguchi, K.; Yagishita, A.; Nomura, M.; Tada, M.; Iwasawa, Y. *Phys. Chem. Chem. Phys.* **2011**, *13*, 15833.

(26) Borgna, A.; Stagg, S. M.; Resasco, D. E. *J. Phys. Chem. B* **1998**, *102*, 5077.

(27) Uemura, Y.; Inada, Y.; Bando, K. K.; Sasaki, T.; Kamiuchi, N.; Eguchi, K.; Yagishita, A.; Nomura, M.; Tada, M.; Iwasawa, Y. *J. Phys. Chem. C* **2011**, *115*, 5823.

(28) Cowley, J. M. *Phys. Rev.* **1965**, *138*, A1384.

(29) Frenkel, A. I. *Chem. Soc. Rev.* **2012**, *41*, 8163.

(30) Vaarkamp, M.; Miller, J. T.; Modica, F. S.; Koningsberger, D. C. *J. Catal.* **1996**, *163*, 294.

(31) Stakheev, A. Y.; Zhang, Y.; Ivanov, A. V.; Baeva, G. N.; Ramaker, D. E.; Koningsberger, D. C. *J. Phys. Chem. C* **2007**, *111*, 3938.

(32) Siani, A.; Wigal, K. R.; Alexeev, O. S.; Amiridis, M. D. *J. Catal.* **2008**, *257*, 16.

(33) Burch, R. *J. Catal.* **1981**, *71*, 348.

(34) Singh, J.; Nelson, R. C.; Vicente, B. C.; Scott, S. L.; van Bokhoven, J. A. *Phys. Chem. Chem. Phys.* **2010**, *12*, 5668.

(35) Serrano-Ruiz, J. C.; Huber, G. W.; Sánchez-Castillo, M. A.; Dumesic, J. A.; Rodríguez-Reinoso, F.; Sepúlveda-Escribano, A. *J. Catal.* **2006**, *241*, 378.

(36) Arteaga, G. J.; Anderson, J. A.; Rochester, C. H. *J. Catal.* **1999**, *184*, 268.